Computers and Fluids 000 (2018) 1–13

Contents lists available at ScienceDirect

Computers and Fluids

journal homepage: www.elsevier.com/locate/compfluid

Isogeometric analysis of multi-phase flows with surface tension and with application to dynamics of rising bubbles

J. Yan[a], S. Lin[a], Y. Bazilevs[b], G.J. Wagner[a,*]

[a] Department of Mechanical Engineering, Northwestern University, United States
[b] Department of Structural Engineering, University of California, San Diego, United States

ARTICLE INFO

Article history:
Received 10 February 2018
Revised 30 March 2018
Accepted 13 April 2018
Available online xxx

Keywords:
Multi-phase flows
IGA
RBVMS
Surface tension
Bubble dynamics

ABSTRACT

A novel multi-phase flow formulation using a level-set-based interface-capturing approach is proposed, focusing on addressing numerical challenges associated with the modeling of surface tension. The surface tension is handled through the continuum surface force model. The residual-based variational multiscale (RBVMS) formulation is employed to solve the coupled Navier–Stokes and level-set convection equations. The RBVMS formulation is discretized using either standard low-order finite elements, or Isogeometric Analysis (IGA) based on Non-Uniform Rational B-Splines (NURBS), which are higher-order accurate and smooth. The proposed method is applied to the simulation of 3D bubbles moving in viscous liquids with large density and viscosity ratios representative of common two-phase flow systems. The accuracy of the proposed method is assessed by comparing the results with analytical solutions, experimental data, and computational results, reported in the literature. In all cases IGA showed superior performance to standard finite elements; this superiority is attributed to the higher-order accuracy of IGA and its ability to directly and accurately compute, using smooth NURBS functions, the curvature term, which is a key ingredient the surface tension formulation. For single-bubble rising problems, the proposed approach produced accurate predictions of the terminal bubble shape, velocity and Reynolds number. The advanced nature of the new multi-phase flow formulation is demonstrated with a simulation of merging of two bubbles in the presence of a deforming free-surface.

1. Introduction

Multi-phase flows occur in many natural and industrial processes such as chemical reactions, oil refining, and water boiling [1–3]. Although significant progress has been made in the simulation of complex single-phase flows in recent years, accurate simulation of multi-phase flows still remain a challenge. The challenges mostly stem from adding surface tension, which becomes important for small spatial scales and in the presence of (highly) curved interfaces, to the multi-phase flow model. These challenges are summarized as follows: (i) The interface separating the fluids must be accurately represented without introducing excessive smearing; (ii) Pressure discontinuity across the interface, induced by the surface tension effect, must be approximated in a way that does not introduce spurious flow near the interface; (iii) Surface normal and curvature must be approximated with sufficient accuracy to compute the surface tension terms.

In recent decades, a number of techniques have been developed to simulate complex multi-phase flow problems. These can be classified into two categories based on how the fluid interface motion is handled, and are referred to as the interface-tracking and interface-capturing methods [4,5]. The interface-tracking approaches, including front-tracking methods [6], boundary-integral methods [7], arbitrary Lagrangian–Eulerian (ALE) methods [8], and space–time finite-element methods [9], use a deformable mesh that conforms to the moving interface. The main advantage of interface-tracking methods is their ability to achieve high per-degree-of-freedom accuracy near the interfaces. However, when the interfaces form a singularity or change topology, interface-tracking methods become challenging to apply in practice, and require the development of special techniques (see, e.g., [10]). Automatic merging or break-up of interfaces are especially challenging for interface-tracking techniques, which makes 3D multi-phase flow problems notoriously more difficult to solve using this class of methods.

On the other hand, interface-capturing methods, such as the volume-of-fluid (VOF) method [11], phase-field methods [12–19], diffuse-interface methods [20,21], front-capturing methods [22],

* Corresponding author.
E-mail addresses: jinhui.yan@northwestern.edu (J. Yan), gregory.wagner@northwestern.edu (G.J. Wagner).

https://doi.org/10.1016/j.compfluid.2018.04.017
0045-7930/

and level-set methods [23–29], utilize an auxiliary function defined on the problem domain to describe the interface, and present a practically simpler alternative to the interface-tracking methods. Although interface-capturing methods typically require higher mesh resolution to compensate for lower interface accuracy, these methods are very robust and relatively simple to implement in practice. Because the changes in interface topology do not present a conceptual difficulty for these methods, they have been applied to a broad range of problems including bubble dynamics [30–32], jet atomization [33], and free-surface flows [34–37]. Among these methods, the level-set technique is especially popular due to its ability to represent complex interfaces using a smooth implicit function. In principle, this function can be used not only to separate the two fluids at their interface, but also to compute the interface normal and curvature that are needed to incorporate the surface tension terms in the multi-phase flow model. Accurate calculation of the interface curvature in lower-order level-set approaches is still a difficult task. Several methods have been developed to address this issue, including approaches based on the Height function [38] or Laplace–Beltrami operator [39]. However, these methods are often hard to apply to unstructured-mesh discretizations of geometrically-complex objects, or require interface-mesh generation, which is computationally expensive and defeats the purpose of using interface-capturing techniques in the first place.

In this paper, a level-set-based multi-phase flow formulation using Isogeometric Analysis (IGA) [40,41] and the residual-based variational multiscale (RBVMS) formulation [42] is proposed. Surface tension is included in the formulation, and is handled through the continuum surface force (CSF) model of Brackbill et al. [43]. IGA, which was originally developed for better integration of Computer-Aided Design (CAD) and Finite Element Analysis (FEA) [40,41], has been widely applied to simulate fluid flow [44], solid and structural mechanics [45,45–48], and fluid–structure interaction (FSI) [5,49–56], in many cases showing superior performance and per-degree-of-freedom accuracy over the standard FEA.

One of the advantages of IGA is the higher-order smoothness of the underlying basis functions, which makes IGA naturally suited for the discretization of models involving higher-order differential operators [46,57–61]. In this paper we take advantage of smoothness of the IGA basis functions to directly discretize the Brackbill CSF model, which involves second-order derivatives of the level-set function, and, as a result, requires the underlying discretization to be at least C^1-continuous.

RBVMS was proposed in [42] for the simulation of incompressible turbulent flows. Since then, several research contributions in [44,62–66] have shown that RBVMS yielded accurate solutions on meshes with large-eddy simulation (LES)-level resolution that converged rapidly to the direct numerical simulation (DNS) results. To fully take advantages of these techniques, in the present work, RBVMS and the IGA discretization based on C^1-continuous non-Uniform Rational B-Splines (NURBS) are employed for computing the fluid velocity, pressure, and level-set unknowns in the proposed multi-phase flow framework. The proposed framework may be thought of as an extension of the work presented in [35–37] to include the surface tension model.

The paper is outlined as follows. The governing equations, including level-set method and the Navier–Stokes equation augmented with the CSF model, are presented in Section 2. Section 3 presents the numerical formulation, which includes RBVMS, basics of IGA, time integration, and solution strategies for the coupled fluid and level-set equations. Additionally, we present two enhancements of the level-set methodology: level-set re-distancing and restoration of the mass balance. Numerical results and discussions are presented in Section 4. The performance of linear FEA and quadratic-NURBS-based IGA are thoroughly compared by simulating the problems of level-set convection, interface curvature evaluation, capillary pressure, and rising of a single bubble. Three cases of single-bubble rising are simulated using IGA, and the results are validated using experimental data. In Section 4.5, the merging of two bubbles in the presence of a deforming free surface is simulated using IGA. Conclusions are drawn in Section 5.

2. Governing equations

Let Ω denote the spatial domain occupied by two different fluids. The densities of the two fluids are denoted by ρ_1 and ρ_2, and the dynamic viscosities are denoted by μ_1 and μ_2, respectively. The interface between the two fluids is denoted by Γ_t. In the level-set method, the interface Γ_t is represented implicitly by introducing a scalar level-set field $\phi(\boldsymbol{x}, t)$ and setting

$$\Gamma_t = \{\boldsymbol{x} \in \Omega \mid \phi(\boldsymbol{x}, t) = 0\}. \tag{1}$$

That is, the two fluids are separated by the zero level-set of ϕ. The evolution of the level-set field is governed by the convection equation,

$$\frac{\partial \phi}{\partial t} + \boldsymbol{u} \cdot \nabla \phi = 0, \tag{2}$$

where $\boldsymbol{u}$ is the flow velocity. The fluid properties are distributed using the following interpolation,

$$\rho = \rho_1 H(\phi) + \rho_2 (1 - H(\phi)) \tag{3}$$

$$\mu = \mu_1 H(\phi) + \mu_2 (1 - H(\phi)) \tag{4}$$

where $H(\phi)$ is the Heaviside function defined as

$$H(\phi) = \begin{cases} 0 & \text{if } \phi < 0 \\ 1/2 & \text{if } \phi = 0 \\ 1 & \text{if } \phi > 0 \end{cases}. \tag{5}$$

This procedure results in a "one-fluid" approach to two-phase flow, without the need to explicitly track the interface or to enforce compatibility of the kinematics and tractions across the interface.

With the above distribution of the fluid properties, the Navier–Stokes equations of isothermal, viscous, incompressible flows are adopted for the two-phase fluid model:

$$\rho \frac{\partial \boldsymbol{u}}{\partial t} + \rho \boldsymbol{u} \cdot \nabla \boldsymbol{u} - \nabla \cdot \boldsymbol{\sigma} - \rho \boldsymbol{g} - \boldsymbol{f}_b = \boldsymbol{0}, \tag{6}$$

$$\nabla \cdot \boldsymbol{u} = 0, \tag{7}$$

where p is the fluid pressure, $\boldsymbol{g}$ is the gravitational acceleration vector, $\boldsymbol{\sigma}(\mathbf{u}, p) = -p\boldsymbol{I} + 2\mu\nabla^s \boldsymbol{u}$ is the Cauchy stress, ∇^s is the symmetric gradient, and $\boldsymbol{f}_b$ is the term accounting for the surface tension effect, which will be described in later sections.

3. Numerical formulation

3.1. RBVMS

To numerically approximate the coupled Navier–Stokes and level-set equations, RBVMS is employed. Let $\mathcal{V}^h$ denote the set of discrete trial functions for the velocity, pressure, and level-set unknowns $\{\boldsymbol{u}^h, p^h, \phi^h\}$, and let $\mathcal{W}^h$ denote the set of discrete test functions for the linear momentum, continuity and level-set equations $\{\mathbf{w}^h, q^h, \eta^h\}$. The formulation for multi-phase flows with surface tension is stated as follows: Find $\{\boldsymbol{u}^h, p^h, \phi^h\} \in \mathcal{V}^h$, such that $\forall \{\mathbf{w}^h, q^h, \eta^h\} \in \mathcal{W}^h$,

$$\int_\Omega \mathbf{w}^h \cdot \rho \left(\frac{\partial \boldsymbol{u}^h}{\partial t} + \boldsymbol{u}^h \cdot \nabla \boldsymbol{u}^h - \boldsymbol{g} \right) \mathrm{d}\Omega - \int_\Omega \mathbf{w}^h \cdot \boldsymbol{f}_b \, \mathrm{d}\Omega$$

Please cite this article as: J. Yan et al., Isogeometric analysis of multi-phase flows with surface tension and with application to dynamics of rising bubbles, Computers and Fluids (2018), https://doi.org/10.1016/j.compfluid.2018.04.017

$$+\int_\Omega \nabla \boldsymbol{w}^h : \boldsymbol{\sigma}(\boldsymbol{u}^h, p^h)\ \mathrm{d}\Omega - \int_\Gamma \boldsymbol{w}^h \cdot \mathbf{h}\ \mathrm{d}\Gamma$$
$$+\int_\Omega q^h \nabla \cdot \boldsymbol{u}^h\ \mathrm{d}\Omega$$
$$+\int_\Omega \eta^h \left(\frac{\partial \phi^h}{\partial t} + \boldsymbol{u}^h \cdot \nabla \phi^h\right)\ \mathrm{d}\Omega$$
$$+\sum_{e=1}^{nel}\int_{\Omega^e} \tau_M \left(\boldsymbol{u}^h \cdot \nabla \boldsymbol{w}^h + \frac{\nabla q^h}{\rho}\right) \cdot \boldsymbol{r}_M(\boldsymbol{u}^h, p^h)\ \mathrm{d}\Omega$$
$$+\sum_{e=1}^{nel}\int_{\Omega^e} \rho \tau_C \nabla \cdot \boldsymbol{w}^h r_C(\boldsymbol{u}^h)\ \mathrm{d}\Omega$$
$$-\sum_{e=1}^{nel}\int_{\Omega^e} \tau_M \boldsymbol{w}^h \cdot \left(\boldsymbol{r}_M(\boldsymbol{u}^h, p^h) \cdot \nabla \boldsymbol{u}^h\right)\ \mathrm{d}\Omega$$
$$-\sum_{e=1}^{nel}\int_{\Omega^e} \frac{\nabla \boldsymbol{w}^h}{\rho} : \left(\tau_M \boldsymbol{r}_M(\boldsymbol{u}^h, p^h)\right) \otimes \left(\tau_M \boldsymbol{r}_M(\boldsymbol{u}^h, p^h)\right)\ \mathrm{d}\Omega$$
$$+\sum_{e=1}^{nel}\int_{\Omega^e} \tau_\phi \boldsymbol{u}^h \cdot \nabla \eta^h r_\phi(\phi^h, \boldsymbol{u}^h)\ \mathrm{d}\Omega = 0. \tag{8}$$

In the above equation, the first three lines correspond to the standard Galerkin formulation of Navier–Stokes and level-set equations, while the rest corresponds to the fine scale terms. In the fine scale terms, *nel* denotes the number elements, $\boldsymbol{h}$ denotes the applied traction, and $\boldsymbol{r}_M(\boldsymbol{u}^h, p^h)$, $r_C(\boldsymbol{u}^h)$ and $\boldsymbol{r}_\phi(\phi^h, \boldsymbol{u}^h)$ are the element-interior residuals of the strong-form momentum, continuity and level-set equations. These are given by

$$\boldsymbol{r}_M(\boldsymbol{u}^h, p^h) = \rho \frac{\partial \boldsymbol{u}^h}{\partial t} + \rho \boldsymbol{u}^h \cdot \nabla \boldsymbol{u}^h - \nabla \cdot \boldsymbol{\sigma}(\boldsymbol{u}^h, p^h) - \rho \boldsymbol{g} - \boldsymbol{f}_b, \tag{9}$$

$$\boldsymbol{r}_M(\boldsymbol{u}^h) = \nabla \cdot \boldsymbol{u}^h, \tag{10}$$

$$\boldsymbol{r}_\phi(\phi^h, \boldsymbol{u}^h) = \frac{\partial \phi^h}{\partial t} + \boldsymbol{u}^h \cdot \nabla \phi^h, \tag{11}$$

where τ_M, τ_C and τ_ϕ are the stabilization parameters [55,67–72] given by

$$\tau_M = \left(\frac{4}{\Delta t^2} + \boldsymbol{u}^h \cdot \mathbf{G}\boldsymbol{u}^h + C_I \left(\frac{\mu}{\rho}\right)^2 \mathbf{G} : \mathbf{G}\right)^{-1/2}, \tag{12}$$

$$\tau_C = \frac{1}{tr(\mathbf{G})\tau_M}, \tag{13}$$

$$\tau_\phi = \left(\frac{4}{\Delta t^2} + \boldsymbol{u}^h \cdot \mathbf{G}\boldsymbol{u}^h\right)^{-1/2}, \tag{14}$$

where C_I is a dimensionless positive constant derived from an element-wise inverse estimate [73] (set to 4 in the present work), $\mathbf{G}$ is the element metric tensor defined by $\mathbf{G} = \left(\frac{\partial \xi}{\partial \mathbf{x}}\right)^T \frac{\partial \xi}{\partial \mathbf{x}}$, and $\frac{\partial \xi}{\partial \mathbf{x}}$ is the inverse of the Jacobian of the transformation between the physical element and its parametric counterpart. Note the present formulation uses the same shape functions space for both velocity and pressure. This is not an LBB stable choice, but our RBVMS method provides pressure stabilization in a form similar to that of a pressure stabilizing Petrov–Galerkin (PSPG) scheme.

For a detailed presentation of the RBVMS methodology, readers are referred to the original development in [42]. It should be noted that while RBVMS was developed for LES of turbulent flows, it is also an accurate and robust methodology for stabilized simulations of laminar incompressible flows.

3.2. Surface tension

At the discrete level, in place of its sharp counterpart given by Eq. (5), a regularized version of the Heaviside function H_ϵ is employed:

$$H_\epsilon(\phi) = \begin{cases} 0 & \text{if } \phi < -\epsilon \\ \frac{1}{2}\left(1 + \frac{\phi}{\epsilon} + \frac{1}{\pi}\sin\left(\frac{\phi\pi}{\epsilon}\right)\right) & \text{if } |\phi| \le \epsilon \\ 1 & \text{if } \phi > \epsilon \end{cases}, \tag{15}$$

where $\epsilon \sim O(h)$ defines the local width of the interface between the two fluids. As the mesh is refined, $\epsilon \to 0$. We also define a regularized Dirac delta function δ_ϵ as

$$\delta_\epsilon(\phi) = \frac{dH_\epsilon(\phi)}{d\phi}. \tag{16}$$

The continuum surface force (CSF) model of Brackbill et al. [43] is used to incorporate surface tension into the multi-phase flow formulation. For this, $\boldsymbol{f}_b$ in Eq. (6) is given by

$$\boldsymbol{f}_b = \sigma_s \kappa \delta_\epsilon(\phi)\boldsymbol{n}, \tag{17}$$

where δ_ϵ localizes the surface tension force to the interface. The surface tension coefficient is given by σ_s, which is assumed constant in the present work, and tangential stress (e.g., Marangoni force) is not considered. $\boldsymbol{n}$ is the unit normal vector to the interface given by

$$\boldsymbol{n} = \frac{\nabla \phi}{|\nabla \phi|}, \tag{18}$$

In addition, in Eq. (17), κ is the mean curvature, which can be computed from the level-set field as

$$\kappa = \nabla \cdot \boldsymbol{n} = \frac{|\nabla \phi|^2 \mathrm{Tr}(\boldsymbol{\psi}(\phi)) - \nabla \phi^T \boldsymbol{\psi}(\phi) \nabla \phi}{|\nabla \phi|^3}, \tag{19}$$

where $\boldsymbol{\psi}(\phi)$ is the matrix of second derivatives, or the Hessian, of ϕ.

Remark. Regularization of the Heaviside function puts a requirement on the level-set function to satisfy a so-called signed-distance property. Convecting level-set field may violate mass balance. To enforce the signed-distance property and restore the mass conservation during the simulation, the re-distancing and mass restoring schemes proposed in [36] are utilized in the present work, respectively.

3.3. Basics of Isogeometric Analysis

Some basics of IGA are presented in this section (for a more detailed development, see for example Cottrell et al. [40]). IGA shape functions are typically B-splines and NURBS, motivated by CAD descriptions of geometric models. B-splines are piecewise polynomial curves, constructed by a linear combination of n basis functions of order p and the associated n control points. NURBS are constructed from B-splines. A univariate B-spline is a piecewise polynomial function built upon a knot vector. A knot vector is a non-decreasing sequence of coordinates in the parametric domain denoted by $\boldsymbol{\Xi} = \{\xi_1, \xi_2, \ldots, \xi_{n+p+1}\}$, where ξ_i is the ith knot, n is the number of B-spline basis functions defined on $\boldsymbol{\Xi}$, and p is the polynomial order. If knots are repeated $p+1$ times at the ends of the parametric space, the knots vectors are called *open knots vectors*. Open knots vectors are employed in this work. The interval $[\xi_i, \xi_{i+p+1}]$ is called a knot span. A B-spline basis function is C^∞-continuous inside a knot span, and C^{p-m}-continuous at knots with multiplicity $m \le p$. Given $\boldsymbol{\Xi}$, B-spline basis functions $N_{i,p}$ are defined recursively, starting with piecewise-constant functions ($p = 0$) on each knot span,

$$N_{i,0}(\xi) = \begin{cases} 1 & \text{if } \xi_i < \xi \le \xi_{i+1} \\ 0 & otherwise \end{cases} \tag{20}$$

Please cite this article as: J. Yan et al., Isogeometric analysis of multi-phase flows with surface tension and with application to dynamics of rising bubbles, Computers and Fluids (2018), https://doi.org/10.1016/j.compfluid.2018.04.017

and for $p > 0$, Cox-de Boor recursion is performed, namely,

$$N_{i,p}(\xi) = \frac{\xi - \xi_i}{\xi_{i+p} - \xi_i} N_{i,p-1}(\xi) + \frac{\xi_{i+p+1} - \xi}{\xi_{i+p+1} - \xi_{i+1}} N_{i+1,p-1}(\xi) \tag{21}$$

In order to achieve exact geometric descriptions for objects such as ellipses, circles, and other conic sections, projective transformations of B-splines can be introduced. NURBS are projections of B-splines in $\mathbb{R}^{d+1}$ onto $\mathbb{R}^d$, resulting in a piece-wise rational function. For each B-spline basis function, its NURBS counterpart $R_{i,p}$ is given as

$$R_{i,p}(\xi) = \frac{N_{i,p}(\xi) w_i}{\sum_{\hat{i}=1}^{n} N_{\hat{i},p}(\xi) w_{\hat{i}}} \tag{22}$$

where w_i is a positive weight. NURBS basis functions in higher dimension, such as 3D, are defined by introducing additional knot vectors, $\boldsymbol{\Sigma}$ and Υ, employing a tensor-product construction on the B-spline part of the basis as

$$R^{p,q,r}_{i,j,k}(\xi, \eta, \zeta) = \frac{N_{i,p}(\xi) M_{j,q}(\eta) L_{k,r}(\zeta) w_{ijk}}{\sum_{\hat{i}=1}^{n} \sum_{\hat{j}=1}^{m} \sum_{\hat{k}=1}^{l} N_{\hat{i},p}(\xi) M_{\hat{j},q}(\eta) L_{\hat{k},r}(\zeta) w_{\hat{i}\hat{j}\hat{k}}} \tag{23}$$

where q and r are the polynomial degrees, m and l are the number of univariate B-spline functions, and η and ζ are the parametric coordinates, associated with knot vectors Σ and Υ, respectively.

A NURBS curve $\boldsymbol{C}(\xi)$ is obtained by taking a linear combination of univariate NURBS basis functions from Eq. (22) and control points coordinates $\boldsymbol{B}_i$ as

$$\boldsymbol{C}(\xi) = \sum_{i=1}^{n} R_{i,p}(\xi) \boldsymbol{B}_i \tag{24}$$

Similarly, a NURBS volume patch $\boldsymbol{V}(\xi, \eta, \zeta)$ is constructed analogously as

$$\boldsymbol{V}(\xi, \eta, \zeta) = \sum_{i=1}^{n} \sum_{j=1}^{m} \sum_{k=1}^{l} R^{p,q,r}_{i,j,k} B_{ijk} \tag{25}$$

The unknown field, such as level-set field ϕ, can be expressed as

$$\phi = \sum_{I=1}^{N_s} \psi_I \phi_I \tag{26}$$

where ψ_I is the basis functions (B-splines or NURBS), and N_s is the number of shape functions.

Although the present framework utilizes C^1-continuous quadratic NURBS, it can easily accommodate other representations, such as T-splines or subdivision surfaces [74,75].

3.4. Time integration and coupling strategies

For the time integration of the Navier–Stokes and level-set equations we employ the generalized-α technique, which is a fully-implicit second-order accurate method with control over the dissipation of high frequency modes, provided that the proper α values are chosen. For more details, the readers are referred to [76–78]. At each time step, the combined Navier–Stokes and level-set discrete residuals are converged by means of a monolithic coupling approach, which is also utilized in the free surface simulations in [37,79]. In this coupling approach, at every Newton–Raphson iteration, solution increments of the Navier–Stokes and level-set solutions are computed simultaneously. Linearization of the coupled multi-phase flows equation system takes into account both the Navier–Stokes and level-set subproblems. Although this approach circumvents convergence difficulties associated with a high density ratio, and, as a result, enables robust simulation of multi-phase flows, its efficient numerical implementation is more challenging compared to its staggered counterpart. In the present work, we make use of a matrix-free implementation of the flexible generalized minimum residual (FGMRES) [80,81] technique preconditioned with individual Navier–Stokes and level-set linearized subproblems. The preconditioning reduces the number of FGMRES iterations required for convergence in order to increase the overall efficiency of the algorithm. For a comprehensive discussion of matrix-free and preconditioning techniques, especially for FSI applications, the reader is referred to [35,50].

Table 1
LeVeque deformation problem. Error of IGA and FEM results at $t = T$.

	IGA	FEM
Coarse	0.0137	0.0313
Fine	0.0078	0.0170

4. Numerical examples

4.1. LeVeque deformation problem: comparison between FEA and IGA

We first demonstrate that higher-order accuracy and smoothness of IGA are beneficial for pure level-set convection. The comparison of IGA and FEA on level-set convection can be found in [36]. It shows the convergence rate on level-set convection problems in terms of L_1 error norm is 2 for IGA and 1 for FEM. Here we present an additional comparison by solving a 3D LeVeque deformation problem [82]. This is a well-known benchmark example, tested previously by a number of level-set, volume of fluid and hybrid methods [83–86]. In this example, the computational domain is a unit cube, and a sphere of radius 0.15 initially centered at (0.35, 0.35, 0.35) is convected by the following spatially- and temporally-varying velocity field:

$$u_1 = 2\sin^2(\pi x)\sin(2\pi y)\sin(2\pi z)\cos\left(\frac{\pi t}{T}\right), \tag{27}$$

$$u_2 = -\sin(2\pi x)\sin^2(\pi y)\sin(2\pi z)\cos\left(\frac{\pi t}{T}\right), \tag{28}$$

$$u_3 = -\sin(2\pi x)\sin(2\pi y)\sin^2(\pi z)\cos\left(\frac{\pi t}{T}\right). \tag{29}$$

The flow is reversed for $t > \frac{T}{2}$, and the sphere location and shape are expected to be recovered at $t = T$. In the present work, we first set $T = 2.2$ and simulate the problem using a coarse mesh of $48 \times 48 \times 48$ elements and a fine mesh of $96 \times 96 \times 96$ elements for both C^0-continuous linear FEA and C^1-continuous quadratic NURBS. Figs. 1 and 2 show the isosurface of $\phi = 0$ at $t = \frac{T}{2}$ and $t = T$, respectively. Both FEA and IGA are able to capture the intermediate shape, and recover a close approximation of the sphere final location and shape, which also improve with mesh refinement. However, as is clear from the figures, the IGA results are of higher quality than the FEM results. The error between computed results and analytical results at $t = T$ of FEM and IGA is tabulated in Table 1. The error is quantified as

$$e = \sqrt{\frac{\int_\Omega (\phi^h - \phi_a)^2 \delta_\epsilon(\phi^h)\, d\Omega}{\int_\Omega \delta_\epsilon(\phi^h)\, d\Omega}}, \tag{30}$$

where ϕ_a is the analytical solution. In fact the coarse-mesh IGA results for the final sphere shape are at least as accurate as the fine-mesh FEA results. These results confirm the findings of [36].

In order to further evaluate the performance of IGA, the LeVeque deformation problem with period with $T = 3$ is computed.

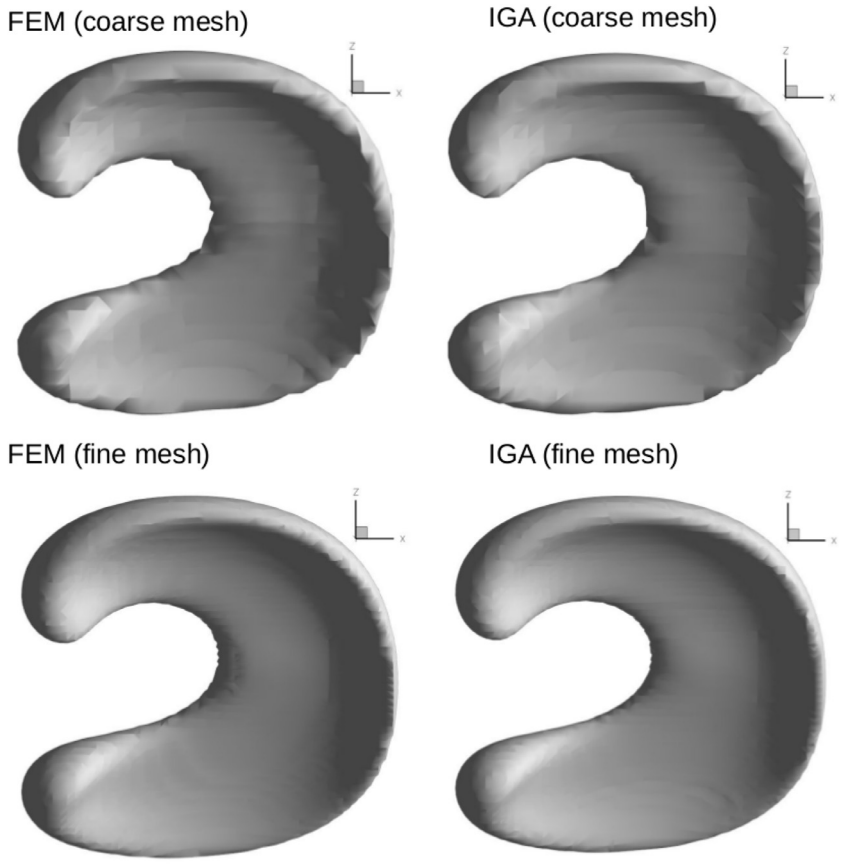

Fig. 1. LeVeque deformation problem. Isosurface of $\phi = 0$ at $t = 0.5T$. (Mesh resolution: $48 \times 48 \times 48$ (coarse) and $96 \times 96 \times 96$ (fine)).

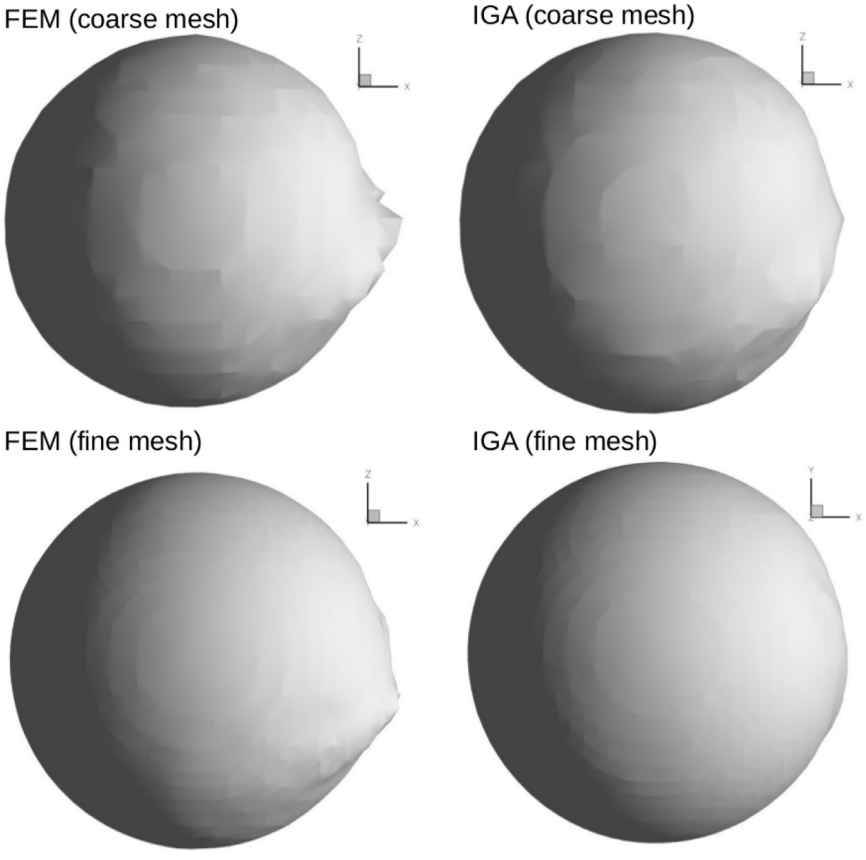

Fig. 2. LeVeque deformation problem. Isosurface of $\phi = 0$ at $t = T$. (Mesh resolution: $48 \times 48 \times 48$ (coarse) and $96 \times 96 \times 96$ (fine)).

Please cite this article as: J. Yan et al., Isogeometric analysis of multi-phase flows with surface tension and with application to dynamics of rising bubbles, Computers and Fluids (2018), https://doi.org/10.1016/j.compfluid.2018.04.017

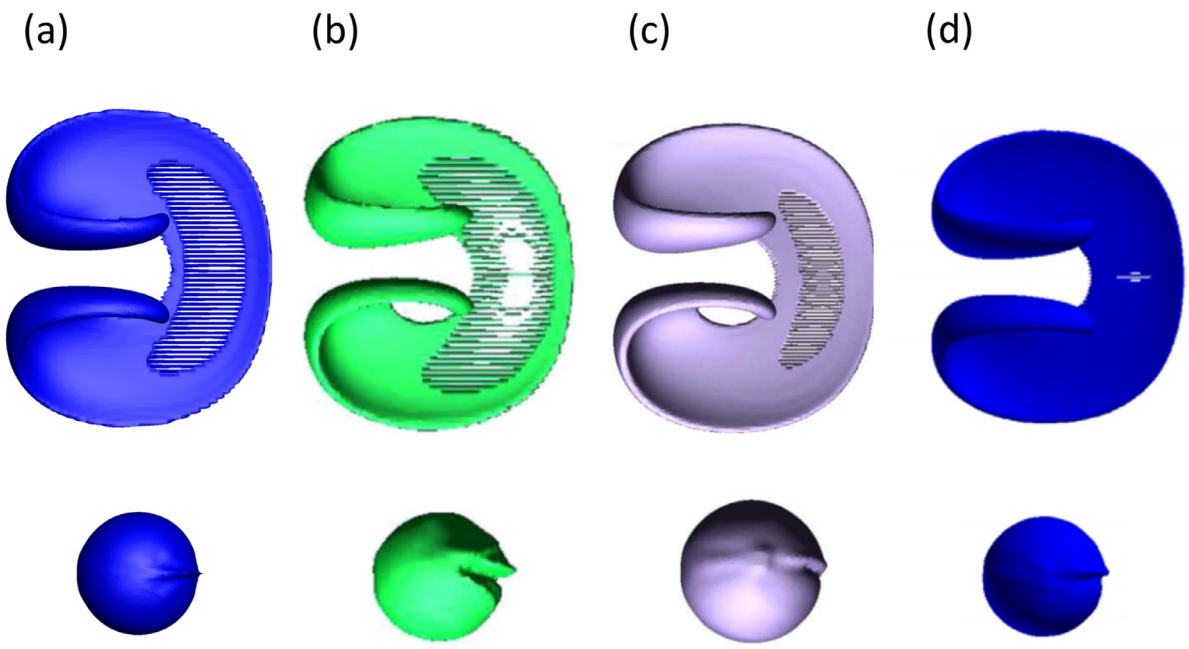

Fig. 3. LeVeque deformation problem with period $T = 3$. Isosurface of $\phi = 0$ at $t = \frac{T}{2}$ (top) and $t = T$ (bottom). (a) Present result (IGA) with resolution 120 × 120 × 120. (b) Coupled level-set and volume-of-fluid method (CLSVOF) with resolution 100 × 100 × 100 from [85]. (c) CLSVOF method with resolution 150 × 150 × 150 from [87]. (d) CLSVOF method with resolution 150 × 150 × 150 from [86].

The isosurface of $\phi = 0$ at $t = \frac{T}{2}$ and $t = T$ generated by IGA, together with some of latest results from the literature, are plotted in Fig. 3. IGA generates quite similar results.

4.2. Curvature evaluation: comparison between FEA and IGA

In order to test the methods for their ability to approximate local surface curvature, we evaluate the curvature at the surface of an implicitly defined sphere of radius of $R = 2$. For this, we consider a domain that is a cube of size $8 \times 8 \times 8$, and initialize the discrete level-set field ϕ^h as the interpolation of ϕ defined by

$$\phi = \sqrt{(x-4)^2 + (y-4)^2 + (z-4)^2} - R. \tag{31}$$

The curvature is calculated by using linear FEA and C^1-continuous quadratic NURBS. In the case of IGA, the curvature Eq. (19) can be evaluated directly for ϕ^h, while for linear FEA, the L_2-projection is adopted to obtain continuous first-order derivative of ϕ^h before invoking Eq. (19). The latter is a typical approach used for curvature computation using linear FEA [30,88]. We use three different element length, $\frac{R}{h} = 5$, $\frac{R}{h} = 10$ and $\frac{R}{h} = 20$. For a perfect sphere, the exact curvature on the sphere surface satisfied the relation $\kappa R = 2$. Since in the present application surface tension is localized to a small band of elements around the interface, it is important to see the accuracy of the curvature evaluation within this region.

Figs. 4 and 5 present scatter plots of κR (curvature times radius) evaluated at all quadrature points of the FEA and IGA meshes, respectively, in the region $|\phi^h| < \epsilon$, where $\epsilon = 2h$ is the interface thickness also used in the bubble-dynamics simulations presented in the following sections. The IGA results are much closer to the analytical solution than their lower-order FEA counterparts. Note that IGA uses 3 × 3 × 3 quadrature points per cell, compared with 2 × 2 × 2 for FEA, and therefore the total number of quadrature points in the interfacial region is larger for IGA.

Curvature error vs. mesh size is plotted in Fig. 6. The error is quantified as

$$e = \sqrt{\frac{\sum_{ip=1}^{N_p} (\kappa_{ip} R_{ip} - 2)^2}{N_p}}, \tag{32}$$

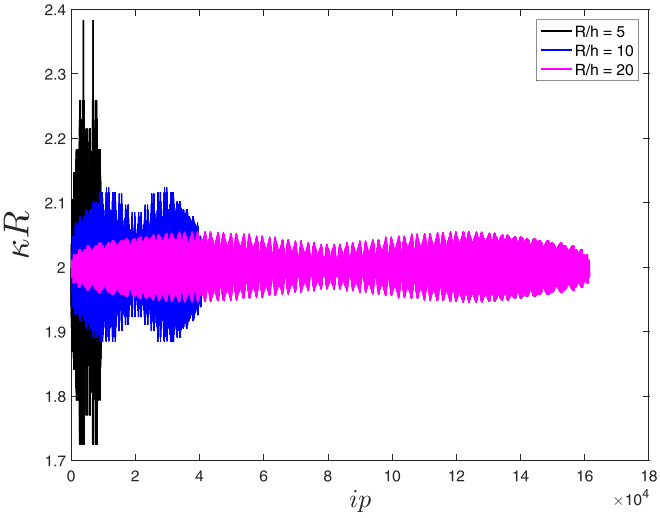

Fig. 4. Curvature evaluation using FEA: κR at quadrature points indexed by ip within the region of $|\phi^h| < 2h$.

where N_p is the number of quadrature points that fall within the region defined by $|\phi^h| < 2h$. The convergence rate of the L_2 norm error is roughly 3 for the quadratic NURBS approximation and 2 for the linear FEM approximation, and the convergence rate of the L_∞ norm error is roughly 2 for the quadratic NURBS approximation and 1 for the linear FEM approximation.

4.3. Static spherical bubble: pressure difference and parasitic currents

To test the formulation of the surface tension, a static problem with an interfacial pressure jump is investigated. A spherical bubble of one phase is immersed in a quiescent fluid of another phase. In the absence of viscosity and gravity, the surface tension is balanced by the pressure difference across the interface, resulting in a static bubble. The pressure difference is given by the Young–

Please cite this article as: J. Yan et al., Isogeometric analysis of multi-phase flows with surface tension and with application to dynamics of rising bubbles, Computers and Fluids (2018), https://doi.org/10.1016/j.compfluid.2018.04.017

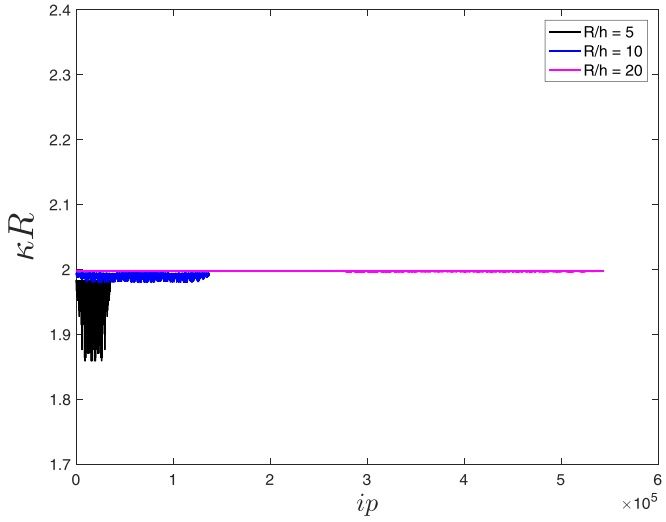

Fig. 5. Curvature evaluation using IGA: κR at quadrature points indexed by ip within the region of $|\phi^h| < 2h$.

Table 2
Static spherical bubble. Maximum velocity $|\mathbf{u}|_{max}$ after one and 50 time steps for a 3D inviscid static bubble computed using different methods. "Francois I" are the results of the balanced-force algorithm with convolution [90]. "Francois II" are the results of the balanced-force algorithm using a height function [90]. "BKZ" are the results of the original CSF paper of Brackbill et al. [43]. "Williams I" are the results using convolved curvatures and a step delta function [91]. "Williams II" are the results using finite-difference normals and a parabolic delta function [91].

Methods	$t = \Delta t$	$t = 50\Delta t$
Francois I	4.87×10^{-3}	1.63×10^{-1}
Francois II	4.02×10^{-3}	4.02×10^{-2}
BKZ	3.49×10^{-1}	2.55×10^{0}
Williams I	1.03×10^{-1}	8.46×10^{-1}
Williams II	8.55×10^{-2}	3.86×10^{-1}
FEA (present)	2×10^{-5}	3.6×10^{-4}
IGA (present)	6×10^{-5}	2.92×10^{-3}

Laplace equation [43]:

$$\Delta p = \sigma_s \kappa = \sigma_s \frac{2}{R}, \tag{33}$$

where R is the bubble radius. In the case of a static bubble, the flow velocities should be exactly zero. However, if the surface tension coefficient is high, and if the representation of the surface forces on the grid has any significant anisotropy, unphysical velocities near the interface are often observed. These unphysical velocities, sometimes called "parasitic currents" [89], depend strongly on many factors such as grid resolution, viscosity, and surface tension.

In the present work, the computational domain is a cube of size $8 \times 8 \times 8$ meshed uniformly with elements of length $h = 0.2$. The bubble of radius $R = 2$ is positioned at the center of the domain. We set the surface tension coefficient $\sigma_s = 73$ and the density ratio $\frac{\rho_2}{\rho_1} = 10$, which are also used in [90]. Time step $\Delta t = 10^{-3}$. A no-penetration boundary condition is applied at all surfaces of the computational domain. Note that the viscosity is zero in this simulation.

The magnitude of unphysical currents after 1 and 50 time steps is reported in Table 2, and compared with those presented in Francois et al. [90] and Williams et al. [91], which use the same problem set-up. Although both FEA and IGA simulations yield spurious velocities, these velocities are orders of magnitude smaller than reported by Francois and Williams, using a balanced force algorithm with numerically computed curvature. This difference can likely be attributed to multiple factors, including the accuracy of the curvature calculation along with the fact that we utilize a fully-coupled velocity-pressure formulation, as opposed to the segregated pressure projection formulation used in previous work. Several previous investigations in [90,92–94] indicate that the magnitude of unphysical currents of this static bubble test case can be reduced to machine precision using balanced-force algorithms, provided that the exact mean curvature is hard coded. In our work, we do not use a balanced-force algorithm, and the numerically computed curvature is used, thus the magnitude does not go to machine precision but still remains quite small. The conclusion is that our formulation, combining RBVMS with a level-set representation, gives residual velocities that compare favorably with other methods, including balanced force formulations with numerically computed curvature. It is surprising that the residual velocities are smaller for FEM than for IGA; this might be attributable to cancellation of errors, or to additional damping from the RBVMS stabilization terms. Below, we show that using IGA can significantly improve the accuracy of the pressure difference.

Refinement studies in FEM and IGA are performed using the coarse mesh with $h = 0.4$, medium mesh with $h = 0.2$, and fine mesh with $h = 0.1$. The computed capillary pressure difference across the interface for all the cases is summarized in Table 3. Pressure contours on the plane corresponding to $z = 4$ for the IGA simulation on a fine mesh are shown in Fig. 7. Pressure along a symmetry line for the IGA and FEA simulations is plotted in Fig. 8. The pressure results show no oscillation, illustrating the robustness

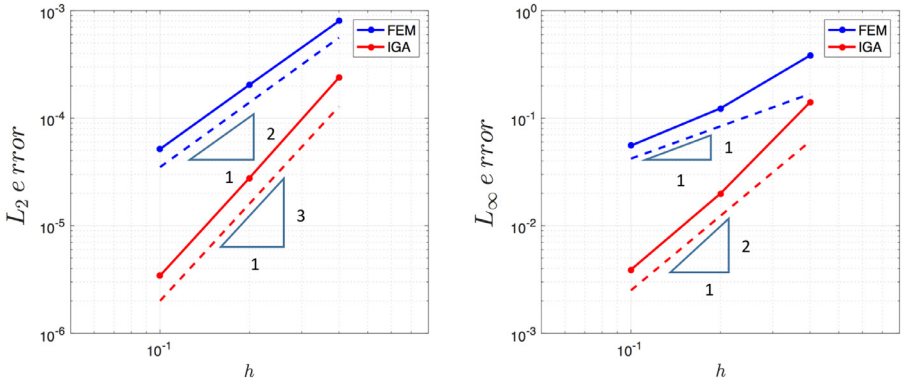

Fig. 6. Curvature error convergence rate of FEA and IGA. Left: L_2 norm of error. Right: L_∞ norm of error.

Table 3
Static spherical bubble. Computed pressure difference across the bubble interface. Note that the exact solution is 73 for this case.

	IGA	FEA
Fine mesh	72.87	73.65
Medium mesh	72.21	74.39
Coarse mesh	71.63	76.93

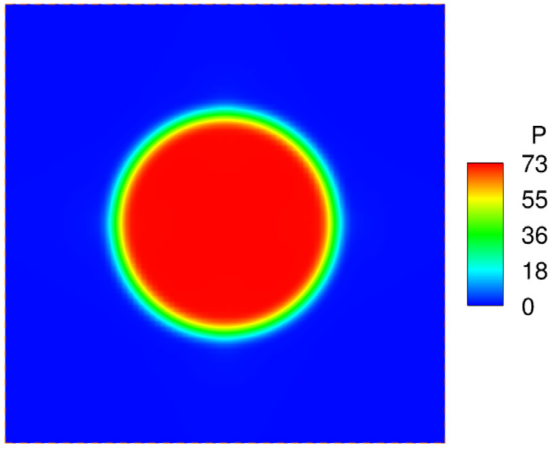

Fig. 7. Static spherical bubble. Pressure contours on a planar cut at $z = 4$ for the IGA simulation.

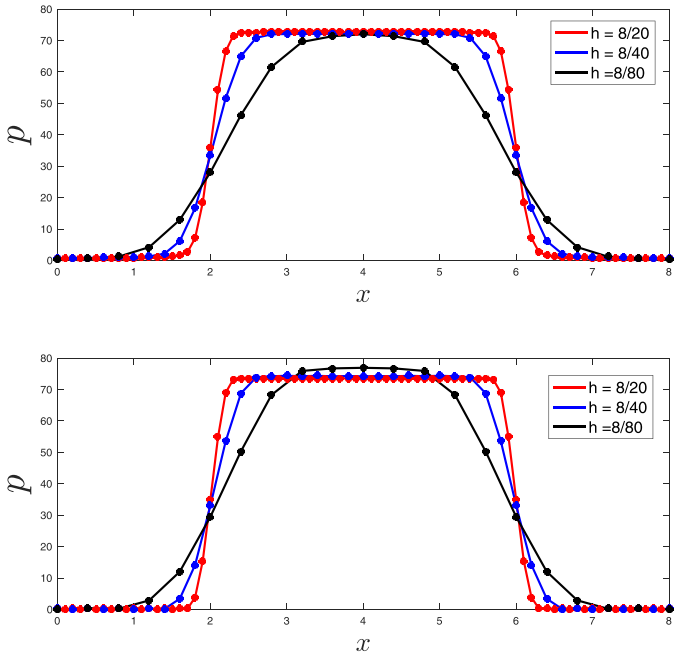

Fig. 8. Static spherical bubble. Pressure along the line from (4,4,0) to (4,4,8) for all cases. Top: IGA results; Bottom: FEA results.

of the RBVMS formulation, and exhibit convergence to a discontinuous profile under with mesh refinement.

4.4. Single rising bubble

In this section, the proposed formulation is used to simulate the problem of a single bubble rising in a quiescent viscous liquid. In what follows, properties with subscripts "1" and "2" are associated with the surrounding liquid and the fluid inside the bubble, respectively. Many experiments have been performed (see, e.g., [95]) investigating the shapes and rise velocities of bubbles in quiescent, viscous liquids. It has been found that the bubble dynamics can be characterized by choosing an appropriate set of dimensionless numbers. Among a large variety of options, in the present work, we use the following dimensionless Archimedes (Ar), Bond (Bo), and Reynolds (Re) numbers defined as

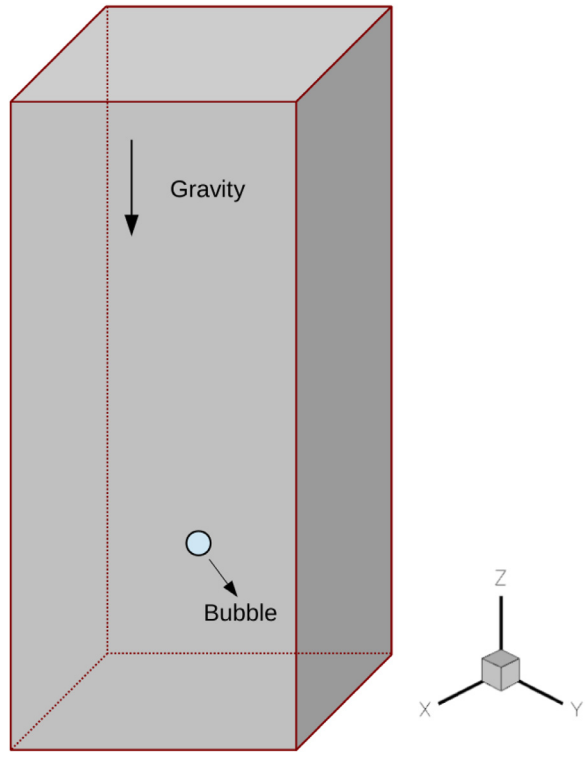

Fig. 9. Single rising bubble. Problem domain and setup.

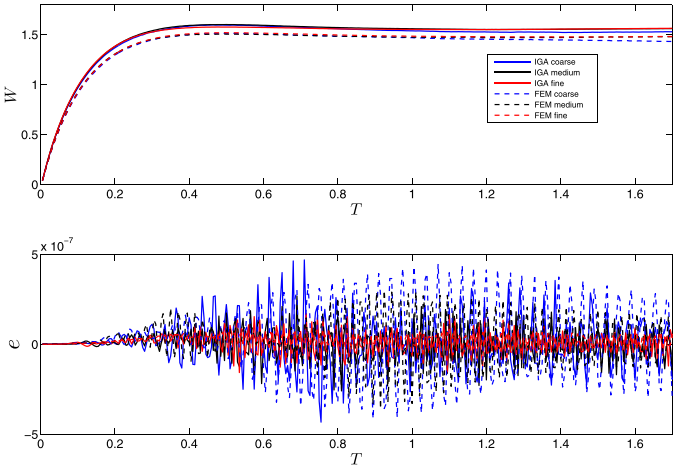

Fig. 10. Single rising bubble. Case B. Top: Time history of bubble-rising speed; Bottom: Time history of relative mass error.

$$Ar = \frac{\rho_1 g^{1/2} D^{3/2}}{\mu_1}, \tag{34}$$

$$Bo = \frac{\rho_1 g D^2}{\sigma}, \tag{35}$$

$$Re = \frac{\rho_1 W_t D}{\mu_1}, \tag{36}$$

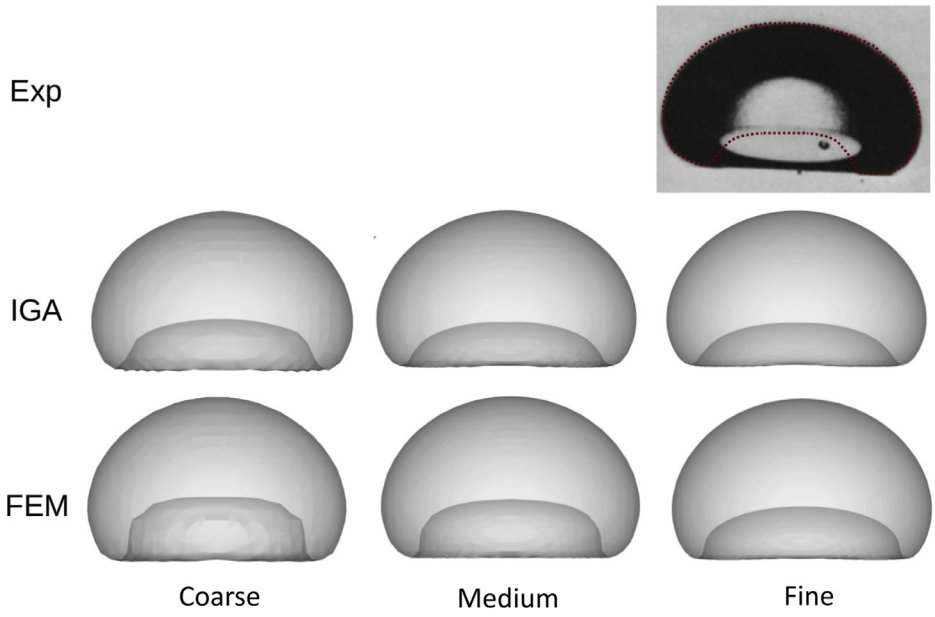

Fig. 11. Single rising bubble. Terminal bubble shape computed using different meshes and discretizations and compared to experimentally-captured images from [95].

Table 4
Single rising bubble. Simulation cases for different Bond and Archimedes numbers.

Cases	D	*Bo*	*Ar*
A	1	17.7	1.671
B	1	243	15.24
C	1	339	30.83

Table 5
Single rising bubble. Element size in the refined region and total number of elements employed in the computations.

	Coarse mesh	Medium mesh	Fine mesh
h	1/20	1/30	1/40
No. of elements	415, 000	1, 444, 000	3, 474, 936

Table 6
Single rising bubble. Terminal *Re* for case B computed using different meshes and discretizations.

	Coarse mesh	Medium mesh	Fine mesh	Experiment
IGA	7.4206	7.5763	7.5862	7.77
FEM	7.0313	7.1554	7.1846	

Table 7
Single rising bubble. All cases computed on the finest IGA mesh. Terminal *Re*.

Cases	Present	Experiment	Hua et al. [10]	Amaya-Bower and Lee [21]
A	0.2593	0.232	0.182	
B	7.5862	7.77	7.605	6.2
C	18.1717	18.3	17.758	15.2

where D is the bubble diameter, g is the gravitational-acceleration magnitude, and W_t is the bubble terminal speed. *Ar* reflects the ratio of buoyancy to viscous force, *Bo* the ratio of buoyancy to surface tension force, and *Re* the ratio of inertial to viscous force. In order to mimic a realistic liquid-gas system (e.g., water and air), the fluid density and viscosity ratios are set to $\frac{\rho_1}{\rho_2} = 1{,}000$ and $\frac{\mu_1}{\mu_2} = 100$, respectively.

The problem setup is shown in Fig. 9. The domain is a box with dimensions $12 \times 12 \times 24$. At the initial time a bubble with diameter $D = 1$ is placed at the location (6, 6, 10.5). Based on previous studies [10,31], the domain is large enough to avoid the effect of side walls. A no-penetration boundary condition is applied at all surfaces of the computational domain. The region $[5.2, 6.8] \times [5.2, 6.8] \times [9, 15.5]$ is meshed with small, uniform elements to better capture the bubble deformation, while the element size is gradually increased toward the boundaries of the computational domain.

Three cases that are commonly used for validation of multi-phase flow numerical formulations are simulated using the dimensionless numbers summarized in Table 4. Case B from the table is chosen for the mesh refinement study. Both IGA and FEA simulations are performed using three different meshes. The element length in the refined region and total number of elements are shown in Table 5. The time history of bubble rising speed and relative mass error are plotted in Fig. 10. The terminal Reynolds number is reported in Table 6, while the terminal bubble shape is shown in Fig. 11. The convergence trend is clearly observed for both FEA and IGA simulations in terms of bubble-rising speed, as well as terminal *Re* and shape. In Fig. 11, comparing the medium and fine FEM results indicates that the final bubble shape has not yet converged for the FEM solution, which may explain the discrepancy between the IGA and FEM terminal velocities seen in Table 6. Mass balance is well satisfied for all cases, with a relative mass error of $O(10^{-7})$. The difference in the bubble shape between the medium and fine mesh is small, which is also consistent with the terminal *Re* number results. In this case, IGA again outperforms FEA: The terminal *Re* in the IGA computations is closer to the experimental value, and the terminal bubble shape in the IGA computations is closer to that in the experimentally-captured image (see Fig. 11).

The rest of the cases are computed using IGA on the finest mesh. Fig. 12 shows the time history of the bubble-rising speed and relative mass errors for all cases. Table 7 and Fig. 13 show the terminal *Re* and bubble shapes, respectively. For case A, surface tension dominates, so the bubble spherical shape is preserved very well, resulting in the smallest *Re* among the cases simulated. For case C, buoyancy plays a more important role than surface tension, resulting in the largest bubble deformation and highest *Re* among the cases simulated. Experimental results from [95],

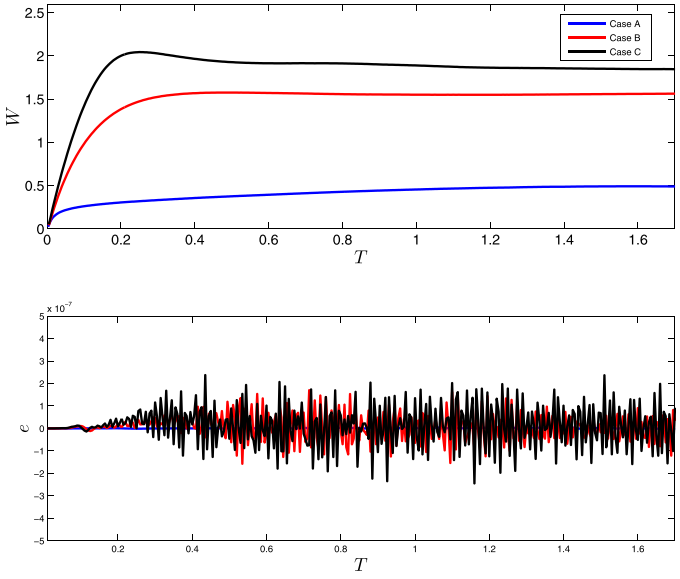

Fig. 12. Single rising bubble. All cases computed on the finest IGA mesh. Top: Time history of bubble-rising speed; Bottom: Time history of relative mass error.

and computational results from Hua et al. [10] using a front-tracking method and Amaya-Bower and Lee [21] using the Lattice–Boltzmann method with a diffuse interface approach, are reported for comparison in Table 7. While for case B the terminal *Re* of Hua et al. [10] is slightly closer to the experimental value than that predicted in the present work, in the remaining cases, the IGA results are closest to the experimental data.

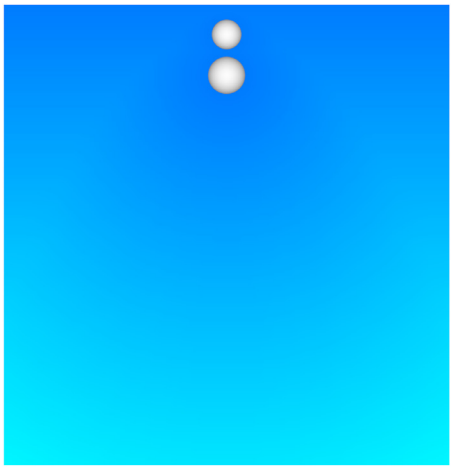

Fig. 14. Bubble merging and interaction with free surface. Initial configuration of the bubbles and free-surface.

4.5. Bubble merging and interaction with free surface

To demonstrate a capability of the proposed methodology to handle complex multi-phase flow scenarios, we simulate buoyancy-driven merging of two bubbles of the same density in the presence of a free surface. The initial positions of the bubbles and the free surface are shown in Fig. 14. The larger bubble with a diameter $D_b = 1$ is centered at (6,6,10.5), while the smaller bubble with a diameter $D_s = 0.8$ is centered at (6,6,11.6). The free-surface, which is initially flat, is located at $z = 12.4$. The density and viscosity ratios are set to $\frac{\rho_1}{\rho_2} = 1000$ and $\frac{\mu_1}{\mu_2} = 100$, respectively. The *Ar* and *Bo* based on the larger bubble are 15.24 and 243, respectively.

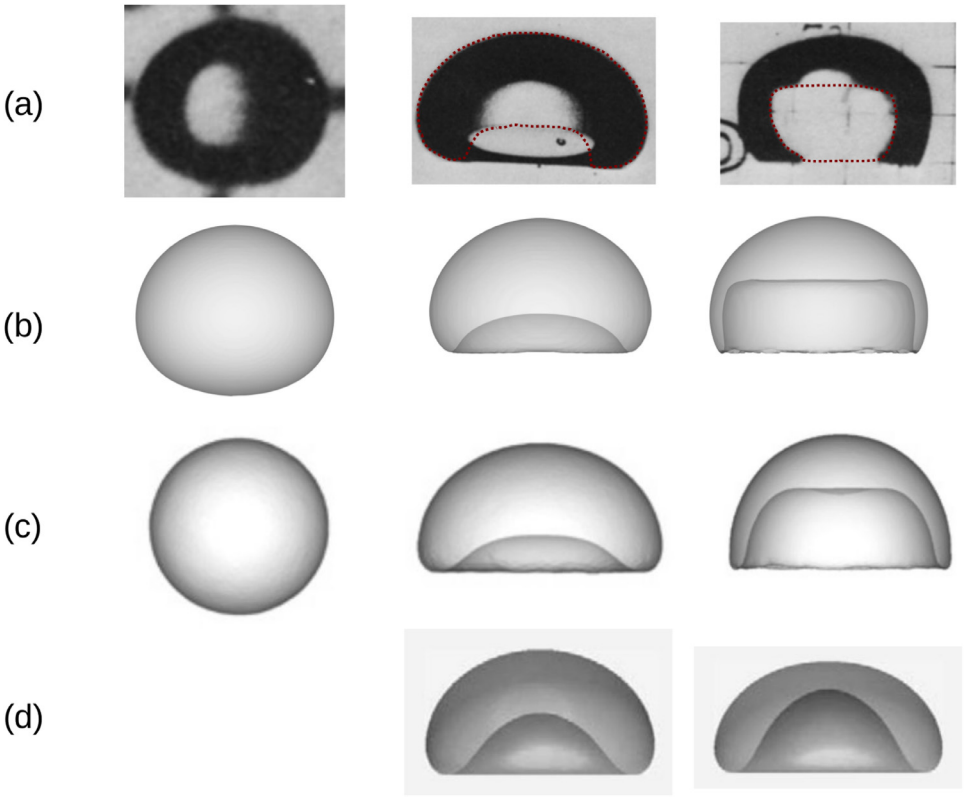

Fig. 13. Single rising bubble. Terminal bubble shape for all cases. (a) Experimental results from [95]; (b) Fine-mesh IGA simulations; (c) Front-tracking method simulations from [10]; (d) Lattice–Boltzmann with diffuse interface simulations from [21].

Please cite this article as: J. Yan et al., Isogeometric analysis of multi-phase flows with surface tension and with application to dynamics of rising bubbles, Computers and Fluids (2018), https://doi.org/10.1016/j.compfluid.2018.04.017

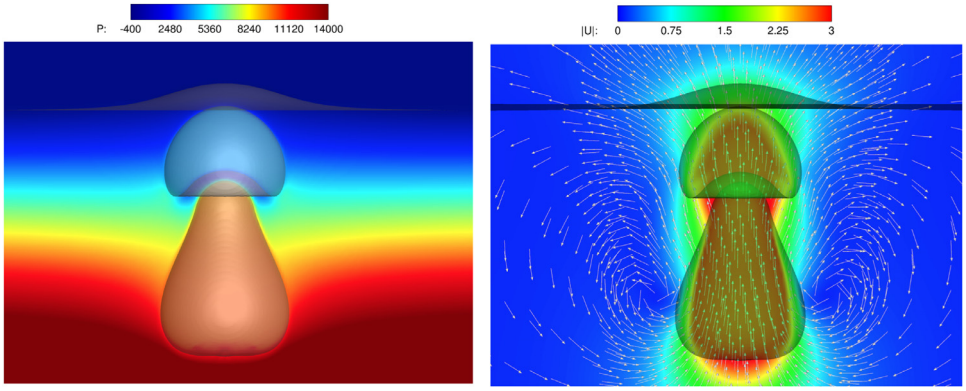

Fig. 15. Bubble merging and interaction with free surface. Left: Pressure contour prior to merging on a planar cut at $y = 6$; Right: Velocity magnitude contour and velocity streamlines on a planar cut at $y = 6$.

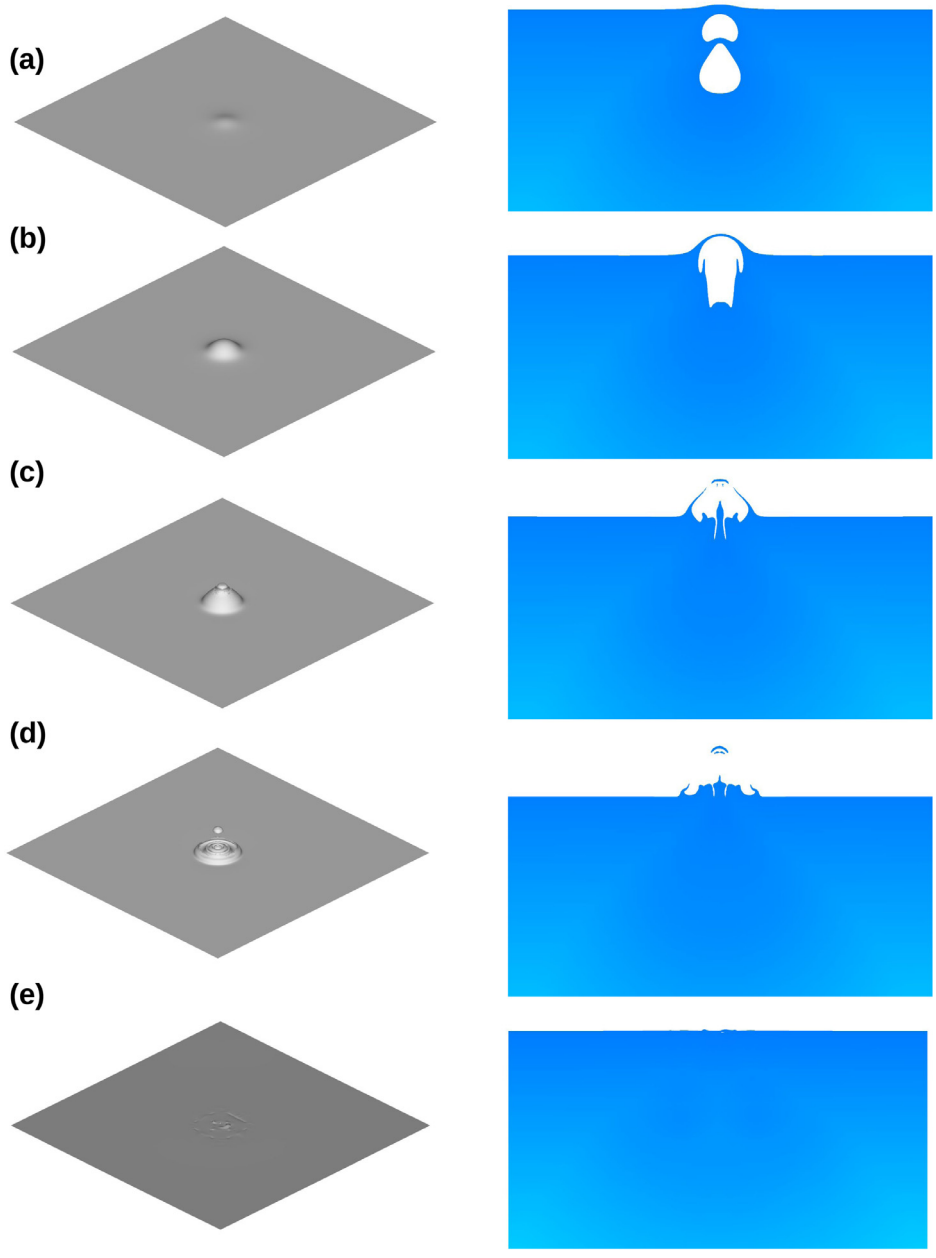

Fig. 16. Bubble merging and interaction with free surface. Snapshots of the system at (a) $t = 0.25$; (b) $t = 0.5$; (c) $t = 0.75$; (d) $t = 1$; (e) $t = 3.49$.

Please cite this article as: J. Yan et al., Isogeometric analysis of multi-phase flows with surface tension and with application to dynamics of rising bubbles, Computers and Fluids (2018), https://doi.org/10.1016/j.compfluid.2018.04.017

The finest IGA mesh from the previous section is also employed in this example. A no-penetration boundary condition is applied at all surfaces of the computational domain.

Fig. 15 shows a snapshot of the bubble deformed shapes superposed with the pressure contours, the flow speed contours and velocity streamlines on a planar cut at $x = 6$ at an instant when the bubbles are about to merge. Fig. 16 illustrates the merging process and its interaction with the free surface. The larger bubble travels in the wake of the smaller one, and rises faster than the smaller bubble. A lower pressure region is observed between the two bubbles in Fig. 15. As time evolves, the upward-moving jet produced by the lower bubble not only affects the upper bubble transients, but also dictates the shape of the lower bubble. When the larger bubble reaches the smaller one, the two bubbles merge. The now single, merged bubble deforms even more as it gets closer to the free surface, and begins displacing the free surface upwards. The liquid sheet between the bubble and free surface thins and eventually breaks producing complex free-surface deformation patterns. Eventually, as the coupled system reaches a steady state, the free surface settles back into a flat configuration.

5. Conclusions

In this paper, a new formulation for multi-phase flows is developed. The formulation is based on the level-set technique and incorporates surface tension. RBVMS is used as the core fluid mechanics formulation. Both standard low-order FEA and NURBS-based IGA are employed to discretize the formulation in space. The use of smooth NURBS functions enables a direct computation of curvature, and as a result, of the surface tension term. In contrast, linear FEA requires an additional projection step to calculate the curvature. numerical evidence is presented, including mesh refinement studies and validation using experimental data, which supports superior performance of the IGA approach. The good performance of IGA is mainly due to the higher-order accuracy of the technique, and the ability to directly and accurately compute, using smooth NURBS functions, the curvature term, which is a key ingredient the surface tension formulation. In addition, the proposed formulation significantly reduces the so-called “parasitic currents” that are present in the classical numerical formulations of multi-phase flows, using numerical computed mean curvature. There is extra computational cost for IGA compared with FEM when using the same number of points, for two reasons: IGA requires more quadrature points for accurate integration, and the support of the IGA basis functions is larger. But as we have shown, a coarse IGA mesh can produce the same and occasionally superior accuracy compared to FEM on a fine mesh. The last numerical example illustrates the power of the proposed methodology on a challenging example involving two bubbles merging in the presence of a deforming free surface.

Acknowledgments

The support of this research by the National Science Foundation under CPS-1646592 for G.J. Wagner and a Graduate Research Fellowship under DGE-1324585 for S.E. Lin is gratefully acknowledged. Y. Bazilevs was partially supported by the ARO Grant no. W911NF-14-1-0296.

References

[1] Prosperetti A, Crum LA, Commander KW. Nonlinear bubble dynamics. J Acoust Soc Am 1988;83(2):502–14.
[2] Plesset MS, Prosperetti A. Bubble dynamics and cavitation. Annu Rev Fluid Mech 1977;9(1):145–85.
[3] Prosperetti A. Vapor bubbles. Annu Rev Fluid Mech 2017;49:221–48.
[4] Prosperetti A, Tryggvason G. Computational methods for multiphase flow. Cambridge University Press; 2009.
[5] Tezduyar TE. Finite element methods for flow problems with moving boundaries and interfaces. Arch Comput Methods Eng 2001;8:83–130. doi:10.1007/BF02897870.
[6] Unverdi SO, Tryggvason G. A front-tracking method for viscous, incompressible, multi-fluid flows. J Comput Phys 1992;100(1):25–37.
[7] Best J. The formation of toroidal bubbles upon the collapse of transient cavities. J Fluid Mech 1993;251:79–107.
[8] Hughes TJR, Liu WK, Zimmermann TK. Lagrangian–Eulerian finite element formulation for incompressible viscous flows. Comput Methods Appl Mech Eng 1981;29:329–49.
[9] Tezduyar TE, Behr M, Liou J. A new strategy for finite element computations involving moving boundaries and interfaces – the deforming-spatial-domain/space–time procedure: I. The concept and the preliminary numerical tests. Comput Methods Appl Mech Eng 1992;94(3):339–51. doi:10.1016/0045-7825(92)90059-S.
[10] Hua J, Stene JF, Lin P. Numerical simulation of 3d bubbles rising in viscous liquids using a front tracking method. J Comput Phys 2008;227(6):3358–82.
[11] Hirt CW, Nichols BD. Volume of fluid (VOF) method for the dynamics of free boundaries. J Comput Phys 1981;39:201–25.
[12] Jacqmin D. Calculation of two-phase Navier–Stokes flows using phase-field modeling. J Comput Phys 1999;155(1):96–127.
[13] Liu J. Thermodynamically consistent modeling and simulation of multiphase flows; Ph.D. thesis; 2014.
[14] Lorenzo G, Scott M, Tew K, Hughes T, Gomez H. Hierarchically refined and coarsened splines for moving interface problems, with particular application to phase-field models of prostate tumor growth. Comput Methods Appl Mech Eng 2017;319:515–48.
[15] Gómez H, Calo VM, Bazilevs Y, Hughes TJ. Isogeometric analysis of the Cahn–Hilliard phase-field model. Comput Methods Appl Mech Eng 2008;197(49–50):4333–52.
[16] Bueno J, Gomez H. Liquid-vapor transformations with surfactants. Phase-field model and isogeometric analysis. J Comput Phys 2016;321:797–818.
[17] Gomez H, Hughes TJ. Provably unconditionally stable, second-order time-accurate, mixed variational methods for phase-field models. J Comput Phys 2011;230(13):5310–27.
[18] Gonzalez-Ferreiro B, Gomez H, Romero I. A thermodynamically consistent numerical method for a phase field model of solidification. Commun Nonlinear Sci Numer Simul 2014;19(7):2309–23.
[19] Gomez H, Reali A, Sangalli G. Accurate, efficient, and (iso) geometrically flexible collocation methods for phase-field models. J Comput Phys 2014;262:153–71.
[20] Yue P, Feng JJ, Liu C, Shen J. A diffuse-interface method for simulating two-phase flows of complex fluids. J Fluid Mech 2004;515:293–317.
[21] Amaya-Bower L, Lee T. Single bubble rising dynamics for moderate Reynolds number using lattice Boltzmann method. Computers Fluids 2010;39(7):1191–207.
[22] Shirani E, Ashgriz N, Mostaghimi J. Interface pressure calculation based on conservation of momentum for front capturing methods. J Comput Phys 2005;203(1):154–75.
[23] Sussman M, Almgren AS, Bell JB, Colella P, Howell LH, Welcome ML. An adaptive level set approach for incompressible two-phase flows. J Comput Phys 1999;148(1):81–124.
[24] Sussman M, Smereka P, Osher S. A level set approach for computing solutions to incompressible two-phase flow. J Comput Phys 1994;114(1):146–59.
[25] Sethian JA, et al. Level set methods and fast marching methods. J Comput Inf Technol 2003;11(1):1–2.
[26] Osher S, Fedkiw R. Level set methods and dynamic implicit surfaces, 153. Springer Science & Business Media; 2006.
[27] Akkerman I. Monotone level-sets on arbitrary meshes without redistancing. Comput Fluids 2017;146:74–85.
[28] Akkerman I., Eikelder M.t. Toward free-surface flow simulations with correct energy evolution: an isogeometric level-set approach with monolithic time-integration. arXiv:180108759 2018.
[29] Yan J, Yan W, Lin S, Wagner G. A fully coupled finite element formulation for liquid–solid-gas thermo-fluid flow with melting and solidification. Comput Methods Appl Mech Eng 2018.
[30] Nagrath S, Jansen KE, Lahey RT. Computation of incompressible bubble dynamics with a stabilized finite element level set method. Comput Methods Appl Mech Eng 2005;194(42):4565–87.
[31] Tripathi MK, Sahu KC, Govindarajan R. Dynamics of an initially spherical bubble rising in quiescent liquid. Nat Commun 2015;6:6268.
[32] van Sint Annaland M, Deen N, Kuipers J. Numerical simulation of gas bubbles behaviour using a three-dimensional volume of fluid method. Chem Eng Sci 2005;60(11):2999–3011.
[33] Gimenez JM, Nigro NM, Idelsohn SR, Oñate E. Surface tension problems solved with the particle finite element method using large time-steps. Comput Fluids 2016;141:90–104.
[34] Yan J, Deng X, Korobenko A, Bazilevs Y. Free-surface flow modeling and simulation of horizontal-axis tidal-stream turbines. Comput Fluids 2017;158:157–66.
[35] Yan J, Korobenko A, Deng X, Bazilevs Y. Computational free-surface fluid–structure interaction with application to floating offshore wind turbines. Comput Fluids 2016;141:155–74.
[36] Akkerman I, Bazilevs Y, Kees CE, Farthing MW. Isogeometric analysis of free–surface flow. J Comput Phys 2011;230:4137–52.

Please cite this article as: J. Yan et al., Isogeometric analysis of multi-phase flows with surface tension and with application to dynamics of rising bubbles, Computers and Fluids (2018), https://doi.org/10.1016/j.compfluid.2018.04.017

[37] Akkerman I, Bazilevs Y, Benson DJ, Farthing MW, Kees CE. Free-surface flow and fluid–object interaction modeling with emphasis on ship hydrodynamics. J Appl Mech 2012;79:010905.
[38] Lörstad D, Francois M, Shyy W, Fuchs L. Assessment of volume of fluid and immersed boundary methods for droplet computations. Int J Numer Methods Fluids 2004;46(2):109–25.
[39] Bänsch E. Finite element discretization of the Navier-Sstokes equations with a free capillary surface. Numer Math 2001;88(2):203–35.
[40] Cottrell JA, Hughes TJR, Bazilevs Y. Isogeometric analysis. toward integration of CAD and FEA. Wiley; 2009.
[41] Hughes TJR, Cottrell JA, Bazilevs Y. Isogeometric analysis: CAD, finite elements, NURBS, exact geometry, and mesh refinement. Comput Methods Appl Mech Eng 2005;194:4135–95.
[42] Bazilevs Y, Calo VM, Cottrell JA, Hughes TJR, Reali A, Scovazzi G. Variational multiscale residual-based turbulence modeling for large eddy simulation of incompressible flows. Comput Methods Appl Mech Eng 2007;197:173–201.
[43] Brackbill J, Kothe DB, Zemach C. A continuum method for modeling surface tension. J Comput Phys 1992;100(2):335–54.
[44] Yan J, Korobenko A, Tejada-Martínez A, Golshan R, Bazilevs Y. A new variational multiscale formulation for stratified incompressible turbulent flows. Comput Fluids 2017;158:150–6.
[45] Kiendl J, Bletzinger K-U, Linhard J, Wüchner R. Isogeometric shell analysis with kirchhoff–love elements. Comput Methods Appl Mech Eng 2009;198(49):3902–14.
[46] Raknes S, Deng X, Bazilevs Y, Benson D, Mathisen K, Kvamsdal T. Isogeometric rotation-free bending-stabilized cables: statics, dynamics, bending strips and coupling with shells. Comput Methods Appl Mech Eng 2013;263:127–43.
[47] Benson D, Bazilevs Y, Hsu M-C, Hughes T. Isogeometric shell analysis: the Reissner–Mindlin shell. Comput Methods Appl Mech Eng 2010;199(5):276–89.
[48] Benson D, Hartmann S, Bazilevs Y, Hsu M-C, Hughes T. Blended isogeometric shells. Comput Methods Appl Mech Eng 2013;255:133–46.
[49] Yan J, Augier B, Korobenko A, Czarnowski J, Ketterman G, Bazilevs Y. FSI modeling of a propulsion system based on compliant hydrofoils in a tandem configuration. Comput Fluids 2016;141:201–11.
[50] Bazilevs Y, Takizawa K, Tezduyar TE. Computational fluid-structure interaction: methods and applications. John Wiley & Sons; 2013.
[51] Takizawa K, Montes D, Fritze M, McIntyre S, Boben J, Tezduyar TE. Methods for FSI modeling of spacecraft parachute dynamics and cover separation. Math Models Methods Appl Sci 2013;23(02):307–38.
[52] Takizawa K, Tezduyar TE. Multiscale space–time fluid–structure interaction techniques. Comput Mech 2011;48:247–67. doi:10.1007/s00466-011-0571-z.
[53] Takizawa K, Tezduyar TE. Space–time fluid–structure interaction methods. Math Models Methods Appl Sci 2012;22(supp02):1230001. doi:10.1142/S0218202512300013.
[54] Tezduyar TE, Sathe S. Modeling of fluid–structure interactions with the space–time finite elements: solution techniques. Int J Numer Methods Fluids 2007;54:855–900. doi:10.1002/fld.1430.
[55] Tezduyar TE, Sathe S, Keedy R, Stein K. Space–time finite element techniques for computation of fluid–structure interactions. Comput Methods Appl Mech Eng 2006;195:2002–27. doi:10.1016/j.cma.2004.09.014.
[56] Tezduyar TE, Sathe S, Stein K. Solution techniques for the fully-discretized equations in computation of fluid–structure interactions with the space–time formulations. Comput Methods Appl Mech Eng 2006;195:5743–53. doi:10.1016/j.cma.2005.08.023.
[57] Liu J, Dedè L, Evans JA, Borden MJ, Hughes TJ. Isogeometric analysis of the advective Cahn–Hilliard equation: spinodal decomposition under shear flow. J Comput Phys 2013;242:321–50.
[58] Liu J, Landis CM, Gomez H, Hughes TJ. Liquid–vapor phase transition: thermomechanical theory, entropy stable numerical formulation, and boiling simulations. Comput Methods Appl Mech Eng 2015;297:476–553.
[59] Deng X, Korobenko A, Yan J, Bazilevs Y. Isogeometric analysis of continuum damage in rotation-free composite shells. Comput Methods Appl Mech Eng 2015;284:349–72.
[60] Kiendl J, Bazilevs Y, Hsu M-C, Wüchner R, Bletzinger K-U. The bending strip method for isogeometric analysis of Kirchhoff–Love shell structures comprised of multiple patches. Comput Methods Appl Mech Eng 2010;199:2403–16.
[61] Wick T. 2013. Computational Mechanics, published online, doi:10.1007/s00466-013-0866-3
[62] Bazilevs Y, Akkerman I. Large eddy simulation of turbulent Taylor–Couette flow using isogeometric analysis and the residual–based variational multiscale method. J Comput Phys 2010;229:3402–14.
[63] Bazilevs Y, Yan J, de Stadler M, Sarkar S. Computation of the flow over a sphere at re = 3700: a comparison of uniform and turbulent inflow conditions. J Appl Mech 2014;81(12):121003.
[64] Golshan R, Tejada-Martínez AE, Juha M, Bazilevs Y. Large-eddy simulation with near-wall modeling using weakly enforced no-slip boundary conditions. Computers Fluids 2015;118:172–81.
[65] Xu F, Schillinger D, Kamensky D, Varduhn V, Wang C, Hsu M-C. The tetrahedral finite cell method for fluids: immersogeometric analysis of turbulent flow around complex geometries. Comput Fluids 2016;141:135–54.
[66] van Opstal TM, Yan J, Coley C, Evans JA, Kvamsdal T, Bazilevs Y. Isogeometric divergence-conforming variational multiscale formulation of incompressible turbulent flows. Comput Methods Appl Mech Eng 2017;316:859–79.
[67] Brooks AN, Hughes TJR. Streamline upwind/Petrov-Galerkin formulations for convection dominated flows with particular emphasis on the incompressible Navier-Stokes equations. Comput Methods Appl Mech Eng 1982;32:199–259.
[68] Hsu M-C, Bazilevs Y, Calo VM, Tezduyar TE, Hughes TJR. Improving stability of stabilized and multiscale formulations in flow simulations at small time steps. Comput Methods Appl Mech Eng 2010;199:828–40. doi:10.1016/j.cma.2009.06.019.
[69] Takizawa K, Tezduyar TE, Kuraishi T. Multiscale space–time methods for thermo-fluid analysis of a ground vehicle and its tires. Math Models Methods Appl Sci 2015;25(12):2227–55.
[70] Takizawa K, Tezduyar TE, McIntyre S, Kostov N, Kolesar R, Habluetzel C. Space–time VMS computation of wind-turbine rotor and tower aerodynamics. Comput Mech 2014;53:1–15. doi:10.1007/s00466-013-0888-x.
[71] Tezduyar T. Stabilization parameters and local length scales in SUPG and PSPG formulations. In: Proceedings of the Fifth world congress on computational mechanics, Vienna, Austria; 2002. On-line publication: http://wccm.tuwien.ac.at/.
[72] Tezduyar T. Interface-tracking and interface-capturing techniques for computation of moving boundaries and interfaces. In: Proceedings of the fifth world congress on computational mechanics, Vienna, Austria; 2002. On-line publication: http://wccm.tuwien.ac.at/.
[73] Harari I, Hughes TJ. What are C and h? Inequalities for the analysis and design of finite element methods. Comput Methods Appl Mech Eng 1992;97(2):157–92.
[74] Bazilevs Y, Calo VM, Cottrell JA, Evans JA, Hughes T, Lipton S, et al. Isogeometric analysis using t-splines. Comput Methods Appl Mech Eng 2010;199(5):229–63.
[75] Cirak F, Ortiz M, Schroder P. Subdivision surfaces: a new paradigm for thin-shell finite-element analysis. Int J Numer Methods Eng 2000;47(12):2039–72.
[76] Bazilevs Y, Calo VM, Hughes TJR, Zhang Y. Isogeometric fluid–structure interaction: theory, algorithms, and computations. Comput Mech 2008;43:3–37.
[77] Chung J, Hulbert GM. A time integration algorithm for structural dynamics with improved numerical dissipation: the generalized-α method. J Appl Mech 1993;60:371–5.
[78] Jansen KE, Whiting CH, Hulbert GM. A generalized-α method for integrating the filtered Navier–Stokes equations with a stabilized finite element method. Comput Methods Appl Mech Eng 2000;190(3):305–19.
[79] Akkerman I, Dunaway J, Kvandal J, Spinks J, Bazilevs Y. Toward free-surface modeling of planing vessels: simulation of the Fridsma hull using ALE-VMS. Comput Mech 2012;50:719–27.
[80] Saad Y. Krylov subspace methods for solving large unsymmetric linear systems. Math Comput 1981;37(155):105–26.
[81] Saad Y, Schultz M. GMRES: a generalized minimal residual algorithm for solving nonsymmetric linear systems. SIAM J Sci StatComput 1986;7:856–69.
[82] LeVeque RJ. High-resolution conservative algorithms for advection in incompressible flow. SIAM J Numer Anal 1996;33(2):627–65.
[83] Ménard T, Tanguy S, Berlemont A. Coupling level set/vof/ghost fluid methods: validation and application to 3d simulation of the primary break-up of a liquid jet. Int J Multiphase Flow 2007;33(5):510–24.
[84] Enright D, Fedkiw R, Ferziger J, Mitchell I. A hybrid particle level set method for improved interface capturing. J Comput Phys 2002;183(1):83–116.
[85] Wang Z, Yang J, Stern F. A new volume-of-fluid method with a constructed distance function on general structured grids. J Comput Phys 2012;231(9):3703–22.
[86] Zhao Y, Chen H-C. A new coupled level set and volume-of-fluid method to capture free surface on an overset grid system. Int J Multiphase Flow 2017;90:144–55.
[87] Wang Z, Yang J, Koo B, Stern F. A coupled level set and volume-of-fluid method for sharp interface simulation of plunging breaking waves. Int J Multiphase Flow 2009;35(3):227–46.
[88] Jansen KE, Collis SS, Whiting C, Shaki F. A better consistency for low-order stabilized finite element methods. Comput Methods Appl Mech Eng 1999;174(1):153–70.
[89] Tryggvason G, Bunner B, Esmaeeli A, Juric D, Al-Rawahi N, Tauber W, et al. A front-tracking method for the computations of multiphase flow. J Comput Phys 2001;169(2):708–59.
[90] Francois MM, Cummins SJ, Dendy ED, Kothe DB, Sicilian JM, Williams MW. A balanced-force algorithm for continuous and sharp interfacial surface tension models within a volume tracking framework. J Comput Phys 2006;213(1):141–73.
[91] Williams M, Kothe D, Puckett E. Accuracy and convergence of continuum surface tension models. In: Fluid dynamics at interfaces. Cambridge University Press, Cambridge; 1998. p. 294–305.
[92] Abu-Al-Saud MO, Riaz A, Tchelepi HA. Multiscale level-set method for accurate modeling of immiscible two-phase flow with deposited thin films on solid surfaces. J Comput Phys 2017;333:297–320.
[93] Popinet S. An accurate adaptive solver for surface-tension-driven interfacial flows. J Comput Phys 2009;228(16):5838–66.
[94] Abadie T, Aubin J, Legendre D. On the combined effects of surface tension force calculation and interface advection on spurious currents within volume of fluid and level set frameworks. J Comput Phys 2015;297:611–36.
[95] Bhaga D, Weber M. Bubbles in viscous liquids: shapes, wakes and velocities. J Fluid Mech 1981;105:61–85.

Please cite this article as: J. Yan et al., Isogeometric analysis of multi-phase flows with surface tension and with application to dynamics of rising bubbles, Computers and Fluids (2018), https://doi.org/10.1016/j.compfluid.2018.04.017